USGS Award Number G10AP00013
Project Duration: 1/1/2010 – 12/31/2010

Final Technical Report

Imaging Body Wave Attenuation Heterogeneity within the New Madrid Seismic Zone using Local Earthquake

Heather R. DeShon[1] and Shishay T. Bisrat[1]

[1]Center for Earthquake Research and Information
University of Memphis
3876 Central Ave., Suite 1
Memphis, TN 38152-3050

(901) 678-1527, fax (901) 678-4734, hdeshon@memphis.edu
(901) 678-4854, fax (901) 678-4734, stbisrat@memphis.edu

Submitted on May 20, 2011

Abstract

New three-dimensional body wave attenuation images of New Madrid Seismic Zone (NMSZ), derived using local earthquake tomography methods, reveal significant near-source heterogeneity. Although seismic velocity tomography is a common tool used to investigate seismotectonics and crustal structure, a reliable seismic attenuation factor, or Q measurement, can be equally important since Q is more sensitive to temperature, movement of solid-state defects, partial melt, and fluid content. We calculate for Q_P and Q_S using a damped least squares attenuation tomography approach, SIMULQ. We determine P- and S-wave whole path attenuation as measured by spectral decay, or t* values, from good quality local earthquakes recorded by network stations in the NMSZ. The t* values are used much like phase onsets times and inverted to solve for QP and QS in conjunction with pre-determined earthquake locations and P- or S-wave velocity models. Two new and unique datasets presented here include: 1) relative relocations within a 3D P and S model of NMSZ local earthquakes with estimated relative and absolute uncertainties and 2) P- and S-wave t* and corner frequency measurements calculated using a new technique that accounts for site effects in the spectra. Due to unresolved issues with S data, only Q_P is reported here. A wide spectrum of Q values has been reported for the NSMZ seeking to characterize bulk crustal attenuation and understand source processes within the seismogenic zone. The high-resolution attenuation images presented here reveal heterogeneity associated with major tectonic structures that have been previously mapped using velocity tomography. The more stringent waveform quality requirements, necessary to work with spectral data, results in some decrease in resolution for the attenuation images versus the associated velocity images. The joint interpretation of the velocity and tomography methods, still in progress, will provide insight into the role of fluids on seismicity, distribution of physical parameters such as cracks and pores, geometry of pores, etc.

Introduction

Characterizing three-dimensional attenuation structure near the source and regionally provides an additional physical constraint towards understanding how intraplate earthquakes develop far from plate boundaries. Because some rock properties, such as fluid content, have a greater effect on attenuation than velocity [e.g., *Anderson*, 1989], combining three-dimensional (3D) attenuation and seismic velocity models are useful to improve interpretation of the processes and material properties across faults. Additionally, accurate velocity and attenuation measurements are a necessary step to better model wave propagation, compute accurate synthetic seismograms, and model strong ground motion regionally. An outstanding question in intraplate settings, including the New Madrid Seismic Zone (NMSZ), is the relationship between fluids and faulting. High pore fluid pressures can reduce effective normal stress across a fault. Since velocity and attenuation are sensitive to fluid content, integrating 3D velocity and attenuation data provides further insight into seismogenic processes along the NMSZ.

The ability to nucleate and/or propagate rupture is strongly dependent on the mechanical and thermal characteristics and state of stress across a fault, but the NMSZ lies far from the high stress regimes of typical plate boundary faults. The New Madrid Seismic Zone occurs within the Mississippi embayment and may be associated reactivation of faults associated with the ancient Reelfoot Rift boundaries. Low topography, negligible (if debatable) heat flow anomaly [*McKenna et al.*, 2007] and broadly low strain rates [*Newman et al.*, 1999; *Calais et al.*, 2010] are observed. Despite these characteristics of a seemingly stable tectonic environment, the NMSZ is known for generating large earthquakes with a recurrence interval of 1000-500 years [*Tuttle et al.*, 2002]. The Cooperative New Madrid Seismic Zone Network (CNMSN) records more than 200 small magnitude earthquakes every year in the seismic zone, primarily along four distinct seismicity bands (Figure 1). The Axial fault extends in the NE-SW orientation along the central Reelfoot Rift [*Russ*, 1982]. Motion along this fault, and the other NE-SW trending features, is primarily right lateral strike-slip. The Reelfoot Fault extends NW-SE across the Mississippi River [*Russ*, 1982], and reverse motion along this fault is thought to result in formation of Reelfoot Lake and changing flow within the Mississippi River during the 1811-1812 earthquake sequence. Competing hypotheses have been proposed to explain the causative processes of earthquakes in this region based on seismological, geological, hydrological, groundwater, and drill data.

The CNMSN catalog of well-recorded small magnitude seismicity in the NMSZ provides a plethora of data to conduct velocity and attenuation studies at a local scale. The Center for Earthquake Research and Information (CERI) maintains a database of local earthquakes waveforms, hypocenters, and body wave onset times for the NMSZ recorded by a regional seismic network. The study consists of a series of high-resolution earthquake relocation of the CNMSN catalog through 2010 and followed by local earthquake attenuation tomography that has resulted in a new 3D P- and S-wave attenuation (Q_P and Q_S) images of the NMSZ. P- and S-wave amplitude spectra of locally recorded earthquakes in the CERI catalog contain information about heterogeneous body wave attenuation along source-receiver paths. We solve for 3D attenuation structure in the NMSZ region using high-frequency spectral decay, or t*, values. Site corrections are removed from all spectra prior to the t* measurement to account for local site effects and instrument response, following the joint inversion approach of *Bennington et al.*

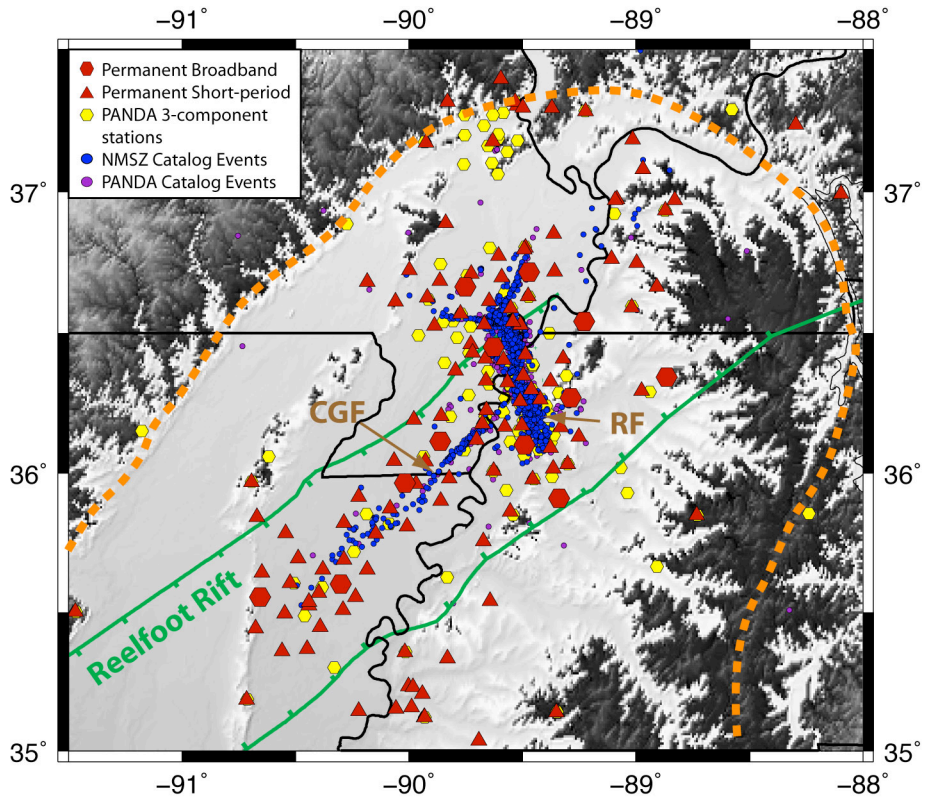

Figure 1: The New Madrid Seismic Zone occurs within the Mississippi embayment (orange line) and may be associated reactivation of faults associated with the ancient Reelfoot Rift boundaries (green lines). A regional network of short-period and broadband stations (red triangles and hexagons) currently monitors the NMSZ. High accuracy earthquakes recorded from 2000 (blue circles) will be used for this study. The temporary PANDA network (yellow hexagons) also provides high quality recordings of local earthquakes (purple circles) from 1989-1992. CGF: Cottonwood Grove Fault & Blythville Arch seismic lineation; RF: Reelfoot fault.

[2008], built upon the SIMUL family of codes [*Evans et al.*, 1994; *Thurber and Eberhart-Phillips,* 1999]. Data collected as part of the 1989-1992 Portable Array for Numerical Data Acquisition (PANDA) [*Chiu et al.*, 1992] (Figure 1) and attenuation tomography using double-difference approaches will be incorporated into a later update to this technical report. Improved resolution along the major New Madrid fault arms allow us to explore the seismic signature of an active intraplate system and characterize the physical properties along and across the faults.

Method and Data

Local earthquake tomography (LET) methods use arrival time residuals to provide both improved earthquake locations in absolute space and 1D, 2D, or 3D seismic velocity information. The algorithm family SIMUL, which we will use for attenuation solutions, calculates the iterative damped least squares solution to the coupled hypocenter-velocity problem and uses an approximate psuedo-bending ray-tracer for computation of theoretical travel times [*Thurber*, 1983; *Eberhart-Phillips*, 1986; *Evans et al.*, 1994]. Velocity and hypocenter is held fixed, and the tomographic inversion for attenuation seeks to reduce t* residuals by iterating Q along the raypath defined by the velocity and hypocenter [*Thurber and Eberhart-Phillips*, 1999].

The method has been successfully used in a wide range of tectonic settings including subduction environments [e.g., *Haberland and Rietbrock*, 2001; *Eberhart-Phillips and Chadwick*, 2002], strike-slip systems [e.g., *Rietbrock*, 2001; *Bennington et al.*, 2008], and volcanic settings [*Hansen et al.*, 2004]. The 3D Q tomography solution uses damping to stabilize the inversion, and absolute Q values may not be fully recovered. Relative Q values and spatial patterns are recovered to the extent of station coverage and inversion resolution and can be compared to other available geophysical and geological data for interpretation purposes.

EARTHQUAKE RELOCATIONS AND VELOCITY MODELS

We use the 3D V_P and V_S models calculated by *Dunn* [2009] using double-difference tomography approaches (Figure 2) [*Zhang and Thurber*, 2003]. The original *Dunn* [2009] study incorporated a subset of PANDA and CNMSN data through 2008, declustered to reduce oversampling. In order to maximize potential t* measurements and to insure the highest resolution hypocenter dataset for comparison with velocity and attenuation models, we have extended the CNMSN dataset through 2010 and performed a series of PANDA and CNMSN catalog relocations using double-difference techniques within the Dunn velocity models [*DeShon et al.*, 2010]. Since hypocenters are fixed in the attenuation inversion, extensive testing was done to constrain the absolute and relative uncertainties associated with this relocated catalog.

PANDA data includes 40 3-component stations recording 435 earthquakes with P and S times. The CNMSN data extends from 1995-2008, includes 74 3-component broadband and short-period recordings of 2230 earthquakes. From this starting datasets, we created a set of highest quality data, defined as having a greatest azimuthal P-wave seperation (GAP)<180º and at minimum 8 P-wave arrivals. A second dataset requiring only 4 P-wave arrivals was also tested. Cross-correlation derived differential times were used for the CNMSN dataset. Absolute and relative error were assessed by computing locations using finite difference (tomoFDD) and pseudo-bending (tomoDD) ray tracing approaches, using jack-knife approaches to test dependence on network geometry, and by comparing solutions for events in common between the 8 arrival and 4 arrival minimum datasets. All tests employed the hierarchical weighting scheme shown in Table 1.

Table 1: DD relocation hierarchical weighting parameters

NITER	WTCCP	WTCCS	WRCC	WDCC	WTCTP	WTCTS	WRCT	WDCT	WTCD	DAMP
3	0.01	0.01	-9	-9	0.1	0.08	-9	-9	10.0	150
3	0.01	0.01	-9	-9	0.1	0.08	8	5	10.0	150
3	0.01	0.01	-9	-9	1.0	0.8	6	5	0.1	200
3	0.01	0.01	-9	-9	1.0	0.8	6	5	0.1	200
3	1.00	0.80	-9	2	0.1	0.08	6	5	0.1	200
3	1.00	0.80	6	2	0.1	0.08	6	5	0.1	200
3	1.00	0.80	6	0.5	0.1	0.08	6	5	0.1	200

* NITER: number of iterations to use the following weights
* WTCCP, WTCCS: weight of cross-correlation P, S differential times
* WTCTP, WTCTS: weight of catalog P, S differential times
* WRCC, WRCT: residual threshold in sec for cross-correlation and catalog data
* WDCC, WDCT: maximum distance [km] between cross-correation, catalog linked pairs
* WTCD: weighting of absolute times, taken as relative to WTCT
* DAMP: damping for relocation using lsqr

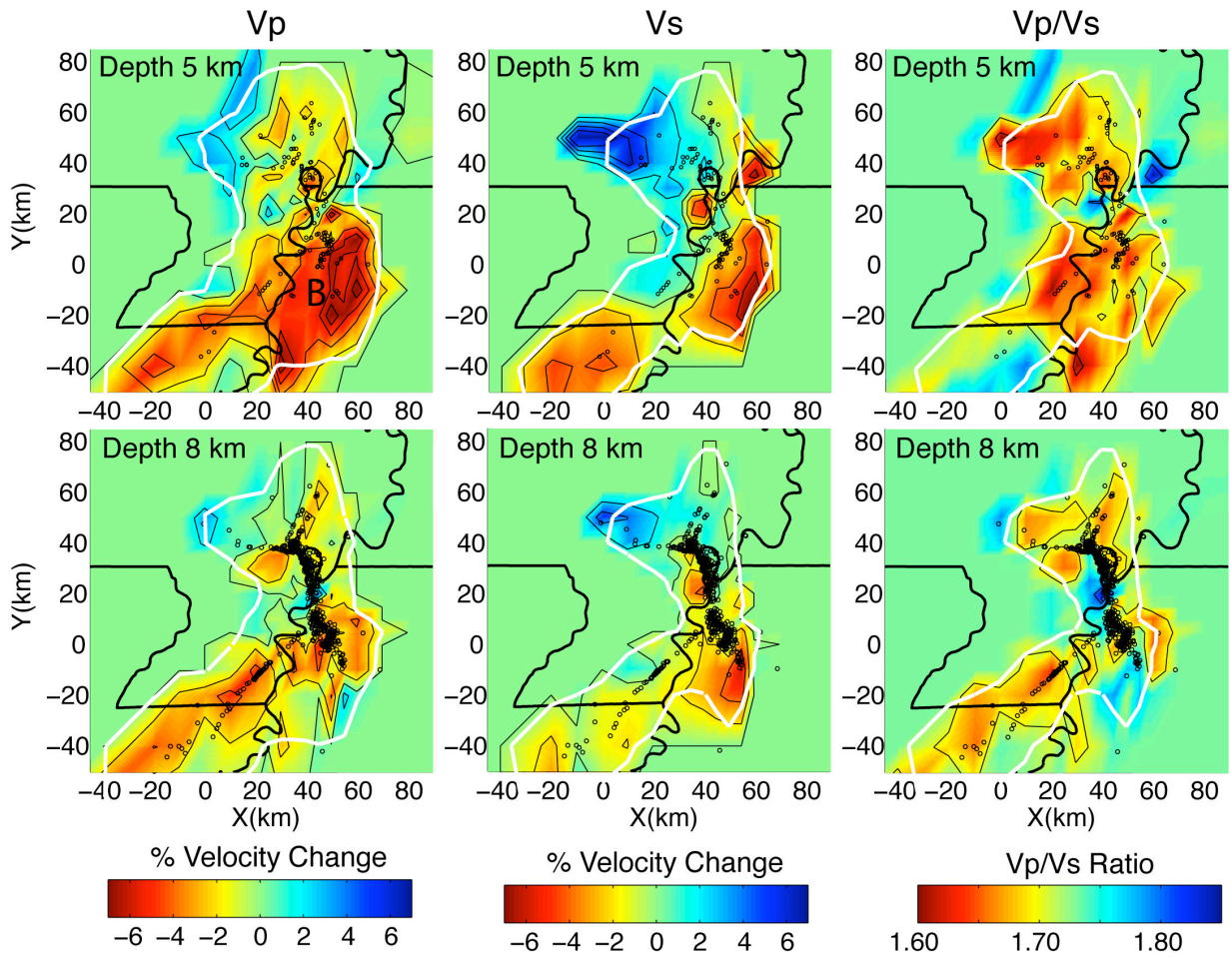

Figure 2. V_P, V_S, and V_P/V_S images for the NMSZ at 5 and 8 km depth [after *Dunn,* 2009]. V_P and V_S are shown as percent change relative to the *Chiu et al.* [1992] starting 1D velocity model. Areas of highest resolution occur within the white contour line. The inversion resolves velocity anomalies of ~ 5 km near regions with high earthquake source density.

We conducted four tests to recover absolute or relative location uncertainty, and each test was done using tomoDD and tomoFDD. Test 1 held all relocation parameters fixed except the minimum number of arrivals, set to 8 or 4. Figure 3 shows the mean change in latitude, longitude and depth for the datasets. Test 2 was the jackknife test to explore location sensitivity to station geometry. One station was dropped and relocations calculated; only stations with a large number of P arrival recordings were removed (28 for CNMSN, 23 for PANDA). Figure 4a,b show the individual jackknife test results and the tabulated means. Test 3 compared tomoDD and tomoFDD solutions as a test of dependency on raytracing technique; results are shown in Figure 5a,b for the 8 and 4 minimum arrival datasets. For test 4, we compared tomoFDD results to relocations calculated using *Benz et al.* [1996] local earthquake tomography method reported in *Powell et al.* [2010]. In this case, many parameters differed, including the velocity model and input phase data distribution. Results for the CNMSN data are shown in Figure 6. Tests 1 and 2 measure relative location uncertainty; tests 3 and 4 are a measure of absolute location uncertainty. We conclude from these tests that the relative (absolute)

uncertainties are on the order of 200-250 (400-600) m epicentrally and 400 (1050) m in depth for the CNMSN data and 200-300 (800-900) m epicentrally and 500 (1700) m in depth for the PANDA data. The relative uncertainty numbers were calculated by rounding up the maximum standard deviation for the FDD results using 8 minimum number of arrivals. For the absolute uncertainty, we simple double and round up the standard deviation of tests 3 and 4.

	CNMSN			PANDA		
DD	Latitude (m)	Longitude (m)	Depth (m)	Latitude (m)	Longitude (m)	Depth (m)
Means	10	6	12	6	1	10
Stddev	473	266	692	61	40	104
FDD	Latitude (m)	Longitude (m)	Depth (m)	Latitude (m)	Longitude (m)	Depth (m)
Means	7	2	2	6	-2	-2
Stddev	264	128	355	42	30	70

Figure 3: Test 1 mean and standard deviations location changes due to changing the minimum number of arrivals. Calculated by taking the 4 minimum P arrival dataset – 8 minimum dataset. Relocations were computed in tomoDD (DD) and in tomoFDD (FDD), and values represent relative location uncertainty.

	CNMSN			PANDA		
DD	Latitude (m)	Longitude (m)	Depth (m)	Latitude (m)	Longitude (m)	Depth (m)
Means	6	6	-23	-8	3	-3
Stddev	367	162	438	361	227	507
FDD	Latitude (m)	Longitude (m)	Depth (m)	Latitude (m)	Longitude (m)	Depth (m)
Means	-2	-3	-4	-2	3	1
Stddev	243	226	414	304	201	479

Figure 4a: Test 2 mean and standard deviations location changes due to removing one station at a time (jack-knife test). Relocations were computed in tomoDD (DD) and in tomoFDD (FDD), and values represent relative location uncertainty.

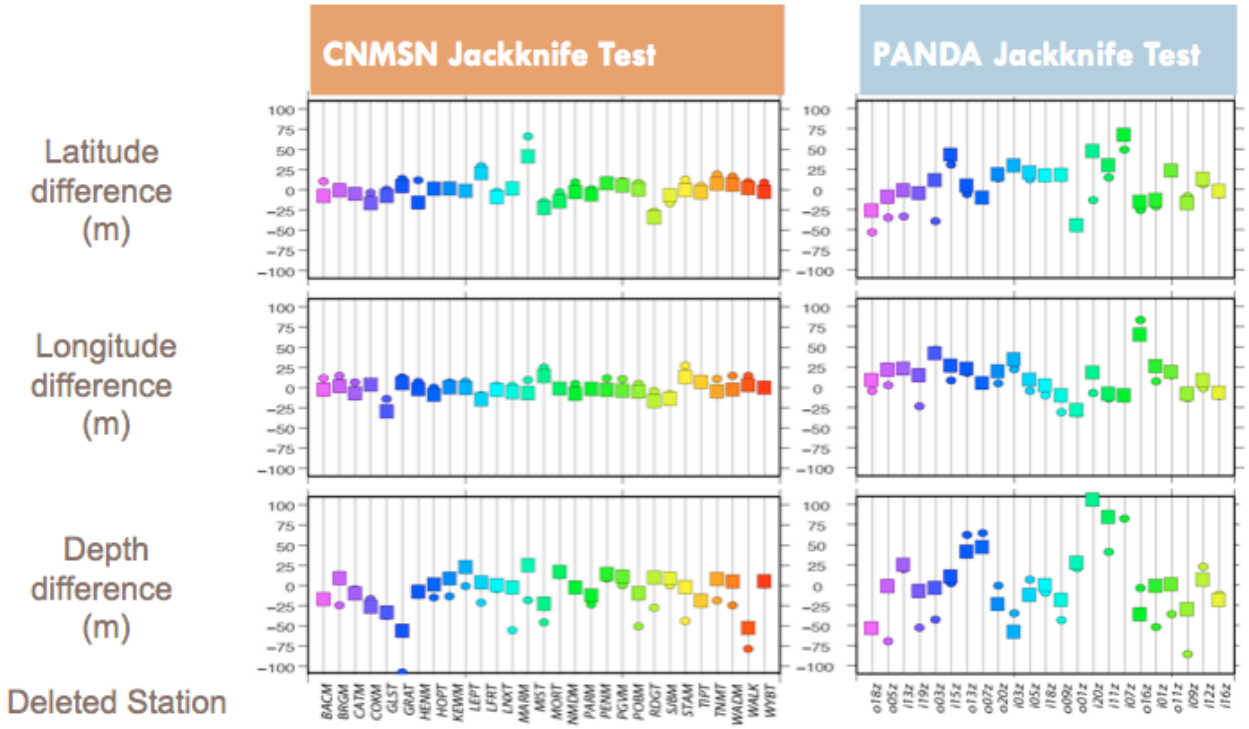

Figure 4b: Test 2 location changes due to removing one station at a time (jack-knife test), separated by station. Relocations were computed in tomoDD (squares) and in tomoFDD (circles), and values represent relative location uncertainty.

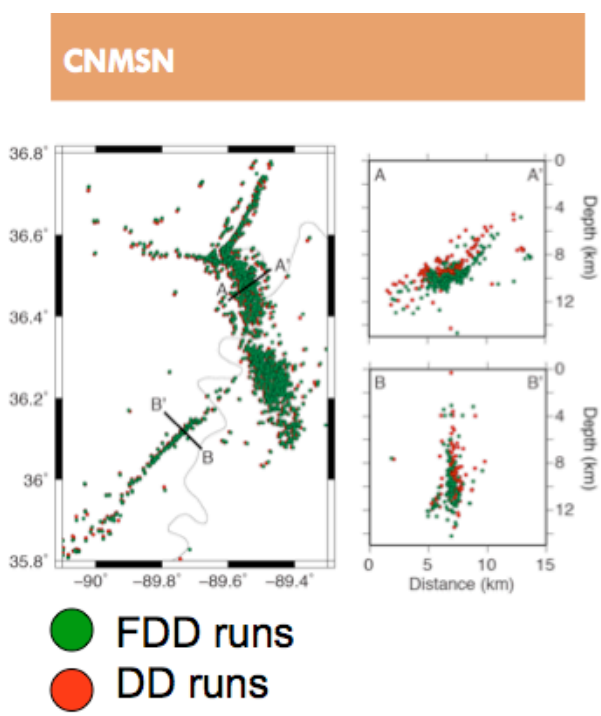

DD – FDD solutions
8 minimum # of arrivals

	Latitude (m)	Longitude (m)	Depth (m)
Mean	156	209	380
Std	619	409	1052

4 minimum # of arrivals

	Latitude (m)	Longitude (m)	Depth (m)
Mean	182	215	331
Std	1568	953	2446

Figure 5a: (left) Map view and cross-sections of CNMSN earthquake locations calculated using tomoDD (red) and tomoFDD (green) with 8 minimum P arrivals. (right) Mean and standard deviations location changes, which represent absolute location uncertainty.

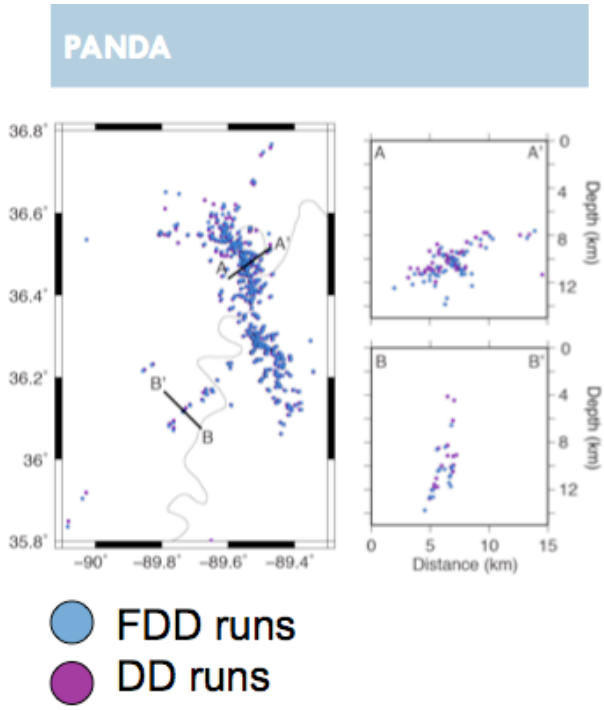

DD – FDD solutions
8 minimum # of arrivals

	Latitude (m)	Longitude (m)	Depth (m)
Mean	227	132	548
Std	529	922	1201

4 minimum # of arrivals

	Latitude (m)	Longitude (m)	Depth (m)
Mean	117	204	550
Std	1726	1239	2477

Figure 5b: (left) Map view and cross-sections of PANDA earthquake locations calculated using tomoDD (purple) and tomoFDD (blue) with 8 minimum P arrivals. (right) Mean and standard deviations location changes, which represent absollute location uncertainty.

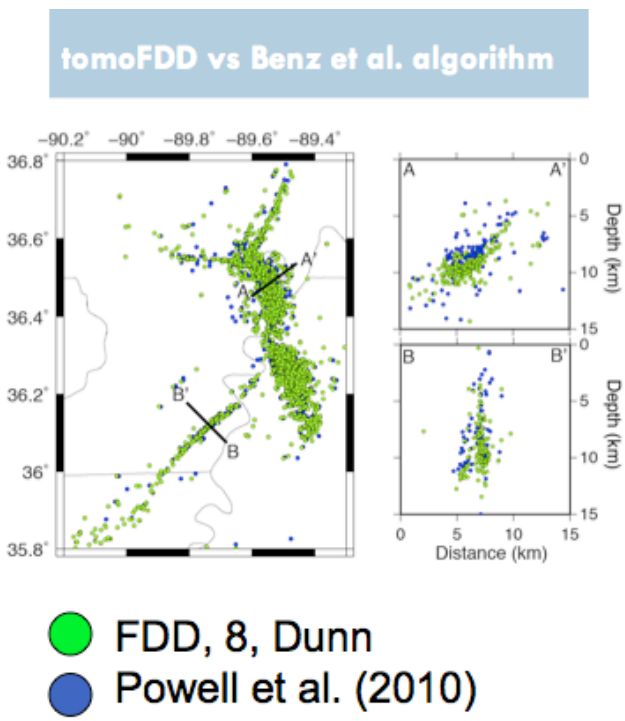

FDD – Powell CNMSN solutions

	Latitude (m)	Longitude (m)	Depth (m)
Mean	-149	-100	887
Std	425	190	762

FDD – Powell PANDA solutions

	Latitude (m)	Longitude (m)	Depth (m)
Mean	13	-130	1253
Std	841	432	1682

Figure 6: (left) Map view and cross-sections of CNMSN & PANDA earthquake locations calculated using tomoFDD (green) and by *Powell et al.* [2010] (blue). (right) Mean and standard deviations location changes, which represent relative location uncertainty.

ATTENUATION TOMOGRAPHY USING t*

The amplitude spectrum of a seismogram of event i recorded at station j is given by

$$A_{ij}(f)=O_j(f)S_i(f)I_i(f)B_{ij}(f) \qquad (1)$$

where A_{ij}, O_j, S_i, I_i, B_{ij} are the amplitude spectrum, source spectrum, site effects, instrument response, and absorption spectrum respectively. The source amplitude spectrum, O_j, has the form

$$O_j = \Omega_o \left[\frac{f_c}{f_c + f}\right]^{\gamma} \qquad (2)$$

where Ω_o, f_c and γ are the low frequency plateau amplitude, the corner frequency and high-frequency decay rate respectively. For $\gamma = 2$, O_j is a Brune source [*Brune*, 1970; 1971] given by

$$O_j = \Omega_o \left[\frac{f_c}{f_c + f}\right]^{2} = \left[\frac{\Omega_o}{\left(1+\left(\frac{f}{fc}\right)^2\right)}\right] \qquad (3).$$

The absorption spectrum B_{ij} is calculated as

$$B_{ij} = e^{\left[-\pi f\left(\frac{T_{ij}}{Q_{ij}}\right)\right]} = e^{[-\pi f t^*_{ij}]} \qquad (4)$$

where T_{ij}, Q_{ij}, and t^*_{ij} are the travel time, dimensionless quality factor and whole path attenuation operator respectively.

Substituting 3 and 4 into equation 1 and removing instrument response gives

$$A_{ij}(f_j) = \left[\frac{\Omega_o}{\left(1+\left(\frac{f}{fc}\right)^2\right)}\right] S(f_j)\, e^{[-\pi f t^*_{ij}]} \qquad (5).$$

Taking the natural logarithm of both sides of equation 5 results in

$$\ln(A(f_j) = \ln(\Omega_o) - \ln\left[1+\left(\frac{f_j}{f_c}\right)\right]^2 + \ln(S(f_j)) + \ln(-\pi f t^*_{ij}) \qquad (6)$$

Many attenuation tomography studies [*Lees and Lindley*, 1994; *Eberhart-Phillips and Chadwick*, 2002; *Stachnik et al.*, 2004] have ignored the site response term, S_i, and solved the observed spectrum for source and attenuation parameters only. *Tsumura et al.* [1996] and *Bennington et al.* [2008] have shown the importance of the site effect, and we use a modified approach of the joint method developed by *Bennington et al.* [2008] to take into account the site effect. Modifications were performed by Jeremy Pesicek, Ninfa Bennington, and Cliff Thurber and remain unpublished at this time.

In the *Bennington et al.* [2008] method, inverting equation 6 for a subset of 6-10 earthquakes solves the source, attenuation and site parameters. The limit on the number of events that can be simultaneously inverted is due to memory required for full inversion of equation 6 and has been extended to allow inversion of up to 100 earthquakes simultaneously [J. Pesicek, personnal communication]. Since equation 6 is nonlinear, Levenberg-Marquardt [*Aster et al*., 2005] is used to solve the inversion problem. The partial derivatives of equation 6 for each parameter are the elements of the Jacobian matrix, **G**. The initial model parameters (Ω, f_c, $S(f_i)$, t^*) are estimated. The perturbation to the model parameters are then calculated using

$$\Delta m = [G^T W G + \varepsilon^2 I]^{-1} G^T W r \qquad (7)$$

where Δ**m** is the model perturbation, **I** is the identity matrix, **r** is the residual between the observed and estimated spectra, and ε is the optimal damping parameter. The damping parameter removes singular values in the inversion matrix and the optimum value gives the best fitting estimated spectra from a range of values. The model is perturbed until the solution converges.

The site response of each station is the average of the site responses determined from each subset. This new average site response is used in equation 6 and Levenberg-Marquardt method is used to estimate f_c for each event, and Ω and t^* for each station.

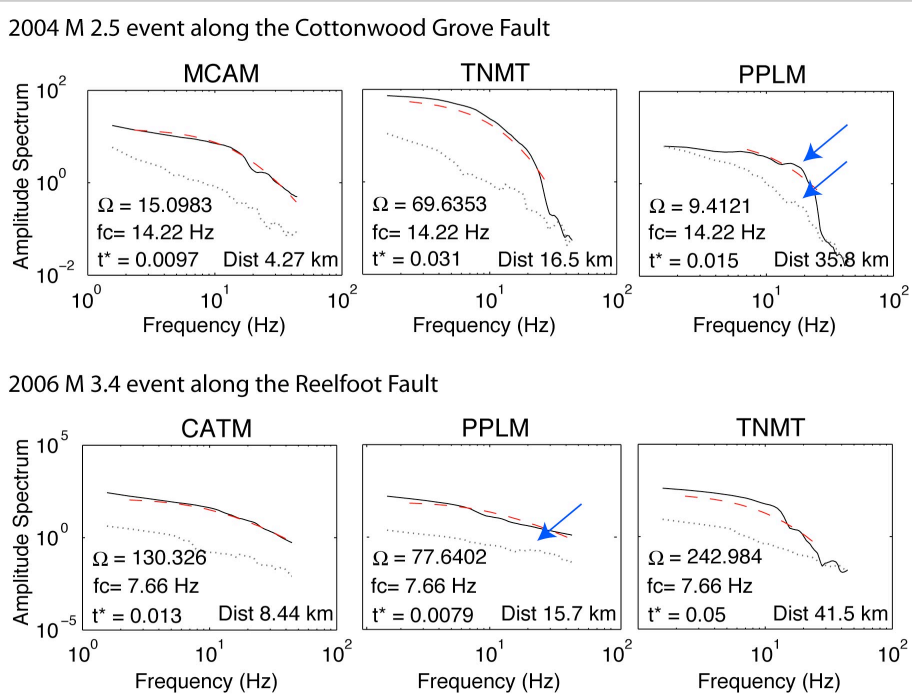

Figure 7: Examples of t* measurements for P-wave arrivals along NMSZ network stations. Shown are the observed spectra (solid black lines) and the estimated spectra (dashed red lines) with the corresponding Ω_o, f_c and t*. The dotted gray line is the observed noise spectra prior to P onset. Unremoved site effects and instrument response can be seen in both earthquake and noise spectra as characteristic spectral peaks present on multiple events (see blue arrows on PPLM spectra).

t* DATA

For the preliminary results presented herein, we use 3-component data recorded by CNMSN stations. The CNMSN stations sample the ground motion at 100 m/sec. The initial data pool consists of 400 microearthquakes with duration magnitudes larger than 2.0 that occurred between 1995 and 2010. Only 291 of these events fulfilled the signal-to-noise, S-P minimum time (1.0 s), and minimum 4 recording station requirements to be included in the final inversion for Q.

P-wave spectra are calculated using the fast fourier transform of a 1.28 sec window of a vertical component of a P-wave that includes a 0.27 sec pre-event noise. A 1.28 sec slice of pre-event noise is used to measure the noise spectra. The P-wave spectra are then divided by the noise spectra to determine the signal-to-noise ratio (quality) of the P-wave signal. A signal-to-noise ratio of greater than 2.3 is good quality and is included in the inversion dataset. Moreover, the SNR value of ≥ 2.3 should occur over at least 10 Hz frequency band.

The amplitude spectra are inverted to determine the whole path attenuation parameter, t*, corner frequency, f_c, low-frequency plateau amplitude, Ω, and site response. Two groups of 100 and 1 group of 91 earthquake events are inverted simultaneously in 15 iterations. The site response is the average of all the site responses computed at a given station (Figure 8). We have found that when inversion is done in batches of 10, the apparent fit to the spectra increases, t* values increase, and f_c increases. We are still exploring ways to stabilize the t* measurements.

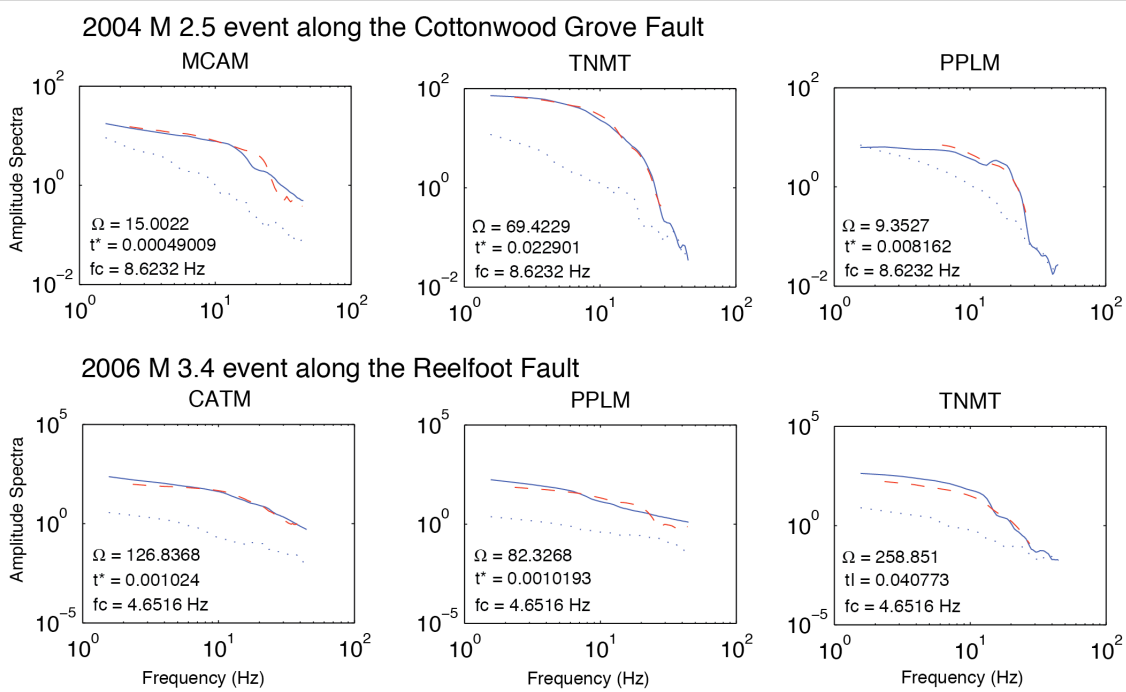

Figure 8a: Examples of t* measurements for P-wave arrivals. Shown are the observed spectra (solid black lines) and the estimated spectra (dashed red lines) with the corresponding Ω_o, f_c and t*. The dotted gray line is the observed noise spectra prior to P onset. Site effects have been calculated and applied using the 100 event modification of *Bennington et al.*, [2008].

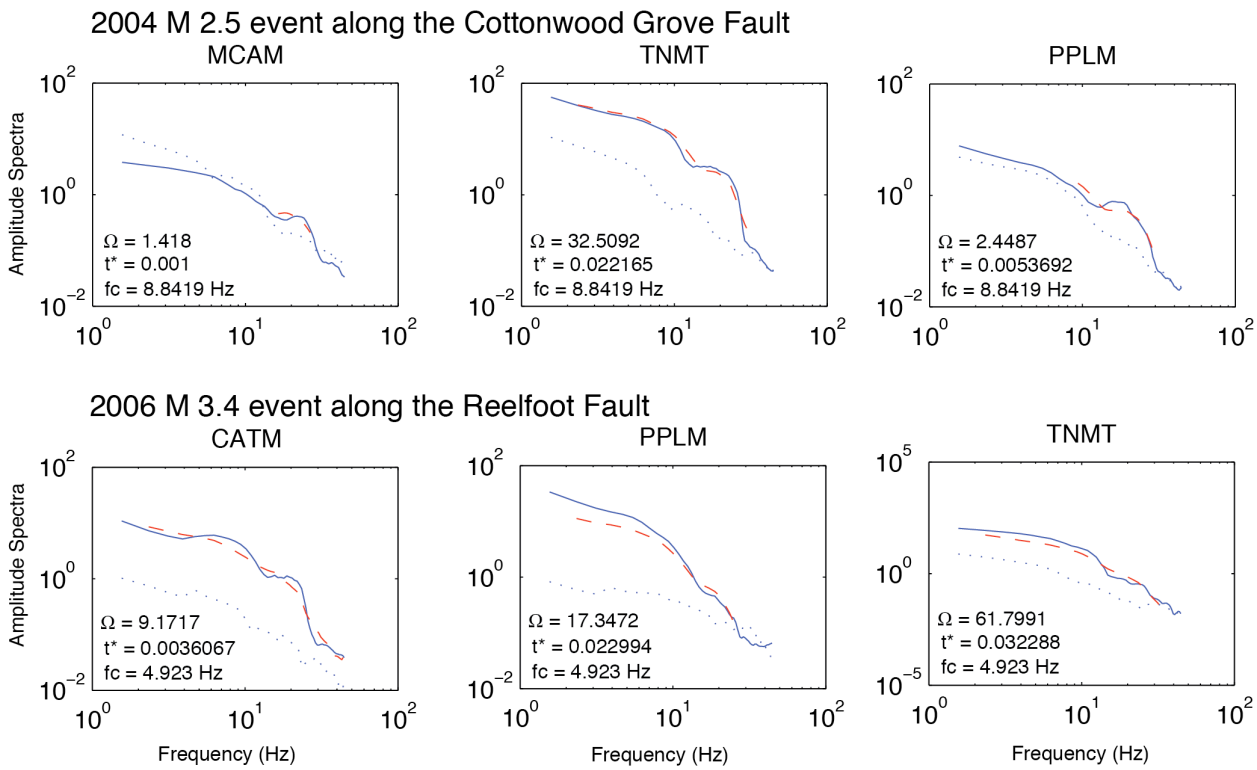

Figure 8b: Examples of t* measurements for S-wave arrivals. Shown are the observed spectra (solid black lines) and the estimated spectra (dashed red lines) with the corresponding Ω_o, f_c and t*. The dotted gray line is the observed noise spectra prior to S onset. Site effects have been calculated and applied using the 100 event modification of *Bennington et al.*, [2008].

Results

Relocations results indicate that the four known seismic lineations exhibit internal complexity (Figure 9). For example, New Madrid north is composed of two parallel faults rather then a single fault (Figure 9A), and seismicity associated with the Axial lineation exhibits temporal changes along strike and becomes spatially more diffuse south of the Axial fault/Bootheel lineament intersection (approximated by the start of cross-section 5 in Figure 9). Seismicity along the southern extension of the Reelfoot fault does not define a dipping plane consistent with thrust faulting, unlike the northern Reelfoot fault (Figure 9C), and is associated with anomalously low P-wave velocities [*Powell et al.*, 2010]. Recent reflection data of the upper 1 km imaged along the Mississippi River indicate that both the north termini of the Reelfoot and Axial faults are characterized by splay faulting [M.B. Magnani, personal communication], while at depth microseismicity is planar.

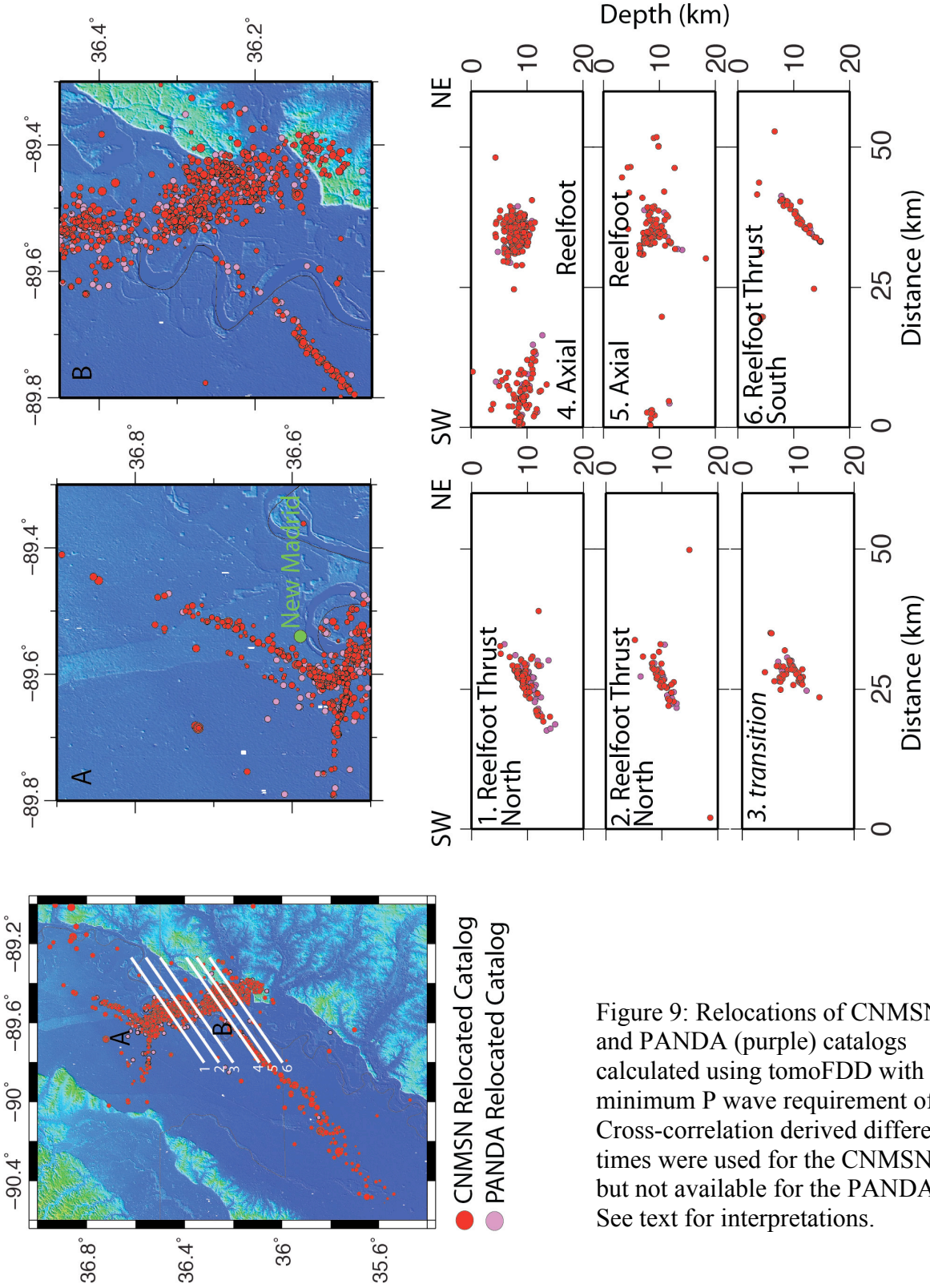

Figure 9: Relocations of CNMSN (red) and PANDA (purple) catalogs calculated using tomoFDD with a minimum P wave requirement of 8. Cross-correlation derived differential times were used for the CNMSN data, but not available for the PANDA data. See text for interpretations.

A recent, high-resolution V_P model [*Dunn*, 2009] (Figure 10) and the computed t* values for CNMSN data are used to determine the Q_P structure. The inversion grid of the attenuation model is the same with the grid used for velocity inversion. The grid spacing is irregular with closely spaced nodes placed in areas of higher ray-path coverage (best resolution). We use tradeoff curves to determine an optimal damping parameter and optimal damping reduction factor. We choose the values 0.023 and 2 for the damping parameter and damping reduction factor respectively. Initial models of constant Q-values of 100, 200, and 300 (Figure 10) were used for Q_P inversion to analyze the sensitivity of the output models to different initial models. No other input parameters were changed. The resulting models have similar features but very different ranges in absolute Q_P values. We stress that these are preliminary models and significant additional work is necessary to assess uncertainty. Q_S modeling is still in the process of being completed.

Discussion and Conclusions

Previous studies of attenuation using high frequency P- and S- and converted waves in the NMSZ have generally found low Q_P and Q_S values on the order of 25-250 and 10-100 respectively [*Liu et al.*, 1994; *Kang and McMechan*, 1994; *Chen et al.*, 1994; *Cong et al.*, 2000; *Hashash and Park*, 2001; *Pujol et al.*, 2002]. These results have generally interpreted to reflect strong attenuation of high frequency energy within the Mississippi embayment sediments. Recent attenuation studies using borehole shot data combined with array measurements of energy trapped within the sedimentary layer suggest that the Mississippi embayment sediments instead amplify high frequency energy and that there is little intrinsic anelastic attenuation within the sediments [*Langston*, 2003; *Langston et al.*, 2005]. These authors suggest that previous Q analyses using spectral ratio and engineering methodology [*Liu et al.*, 1994; *Kang and McMechan*, 1994; *Chen et al.*, 1994; *Cong et al.*, 2000; *Hashash and Park,* 2001; *Pujol et al.*, 2002] were insensitive to intrinsic attenuation and were bias towards low Q values by incorrect wave propagation assumptions. Higher Q values (100-1500) were derived for crustal Q through inversion of spectral decay measurements (t*) using attenuation tomography approaches [*Al-Shukri et al.*, 1988; *Al-Shukri and Mitchell*, 1990], and these results were interpreted to reflect the presence of fluid-filled cracks in the upper crust.

Langston [2003] discussed the difficulty of the effects scattering attenuation and shallow structure waveform propagation from intrinsic anelastic attenuation. We are most interested in measuring intrinsic attenuation near the source faults and within the crust of the NMSZ but recognize that any recording of these events in the embayment may reflect scattering within the unconsolidated sediment layer. *Al-Shukri and Mitchell* [1990] disregarded the effect of scattering and significant attenuation within the shallow (≤1 km) sediments based on their observation that there is no significant variation in Q_P or measured t* values in a north-south direction. *Langston* [2003] and *Langston et al.* [2005] also found the shallow sediments to have low intrinsic attenuation values. Since the most unconsolidated sediment layer is known to thicken to the south, north-south variations should dominate recovered Q values, if present. We make the assumption that scattering attenuation in the P- and S-wave spectra largely effects the site correction term.

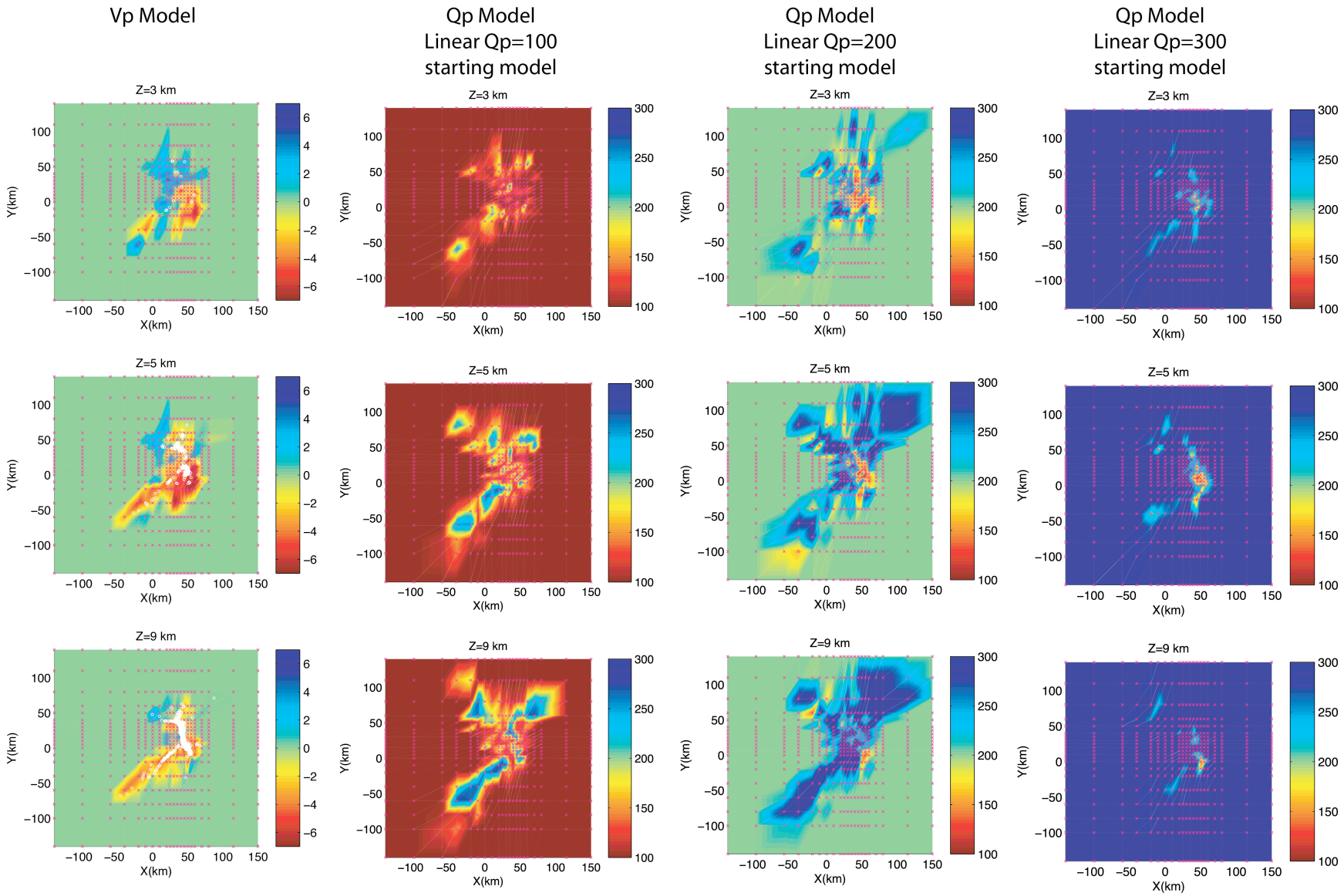

Figure 10: Qp models using different initial Qp starting models. In all cases, the initial input velocity model (far left) and t* data were the same. Earthquake locations within each depth layer are shown by white circles with the Vp model.

The preliminary Q_P attenuation models presented here indicate that most of the major features imaged using velocity tomography are also distinct features in attenuation tomography. The resolution of the attenuation tomography images, however, is lower due to the higher quality requirement of seismic data needed for inversion. The southern end of the Reelfoot fault is shown as a region of low-Q values (high attenuation). Velocity tomography shows this region as low V_P/V_S ratio [*Powell et al*., 2010], and it has produced most of the swarm seismic activity in the last 15 years [*Bisrat et al*., 2011 in review]. All these seismological characteristics are indicative of high pore fluid pressure/ fractured rock environment at seismogenic depths. The second large-scale feature illuminated in the Q_P attenuation structure is a NE-SW trending, high Q (~300) zone at a depth of about 5-10 kms. It coincides with the Cottonwood Grove-Blytheville Arch seismogenic zone.

The values we are seeing in preliminary models span the range of published Q_P values in the NMSZ. Further work testing inversion parameterization and incorporating double-difference methods is needed in order to reach the high-resolution originally proposed. This study is ongoing and will be included as part of a Ph.D. thesis. When completed and published, this technical report will be updated.

Award Bibliography

Bisrat, S.T. and H.R. DeShon (2011), 3-D Seismic Attenuation Structure of the New Madrid Seismic Zone, Seismo. Soc. of Am. Spring Meeting, Memphis, TN, April 2011.

DeShon, H.R., C.A. Powell, M.B. Magnani, and S. Bisrat (2010), Complex Faulting within the New Madrid Seismic Zone, Am. Geophys. Union Fall Meeting, San Francisco, CA, Dec. 2010.

References Cited

Anderson, Don L. (1989), Theory of the Earth. Blackwell Scientific Publications.

Al-Shukri, H. and B. Mitchell (1990), Three-dimensional attenuation structure in and around the New Madrid seismic zone, Bull. Seism. Soc. Am. 80, 615-632.

Al-Shukri, H., B. Mitchell and H.A.A. Ghalib (1988), Attenuation of seismic waves in the New Madrid seismic zone, Seismo. Res. Letts., 59, 133-140.

Aster, R., B. Brochers, and C.H. Thurber (2005), *Parameter Estimation and Inverse Problems*, First. Ed. Elsevier Academic Press, Burlington, Mass.

Bennington, N, C.H. Thurber, S. Roecker (2008) Three dimensional seismic attenuation structure around the SAFOD site, Parkfield, CA, Bull. Seism. Soc. Am., 98, 2934-2947.

Benz, H. M., B. A. Chouet, P. B. Dawson, J. C. Lahr, R. A. Page, and J. A. Hole (1996), Three-dimensional P and S wave velocity structure of Redoubt Volcano, Alaska, *J. Geophys. Res.*, *101*, 8111-8128.

Bisrat, S., H.R. DeShon, and C.A. Rowe (2011), Swarm Activity Within the New Madrid Seismic Zone Identified Using Waveform Cross- Correlation Techniques, Bull. Seism. Soc. Am., in review.

Brune, J. (1970), Tectonic stress and the spectra of seismic shear waves from earthquakes, J. Geophys. Res., 75, 4997-5009.

Brune, J., (1971), Correction, J. Geophys. Res., 76, 5002.

Calais, E., A. M. Freed, R. Van Arsdale and S. Stein (2010), Triggering of New Madrid seismicity by late Pleistocene erosion, *Nature*, 466, 608-612.

Chen, K.-C., J.-M. Chiu, and Y.-T. Yank (1994), Qp-Qs relations in the sedimentary basin of the Mississippi embayment using converted phases, Bull. Seism. Soc. Am., 84, 1861-1868.

Chiu, J. M., A. C. Johnston, and Y. T. Yang (1992). Imaging the active faults of the central New Madrid seismic zone using PANDA array data, Seism. Res. Letters 63, 375-393.

Cong, L., J. Mejia, and B.J. Mitchell (2000), Attenuative dispersion of P waves in and near the New Madrid seismic zone, Bull. Seism. Soc. Am., 90, 679-689.

Dunn, M. (2009), High Resolution Earthquake Locations and Velocity Models in the New Madrid Seismic Zone, Univ. of Memphis, Ph.D. Dissertation.

Eberhart-Phillips, D. (1986), Three-dimensional velocity structure in Northern California Coast Ranges from inversion of local earthquake arrival times, Bull. Seism. Soc. Am., 76, 1025-1052.

Eberhart-Phillips, D., and M. Chadwick (2002), Three-dimensional attenuation model of the shallow Hikurangi subduction zone in the Raukumara Peninsula, New Zealand, J. Geophys. Res., 107, 2033, doi:10.1029/2000JB000046.

Evans, J.R., D. Eberhart-Phillips, and C.H. Thurber (1994), User's manual for SIMULPS12 for imaging Vp and Vp/Vs: a derivative of the Thurber tomographic inversion SIMUL3 for local earthquakes and explosions. U.S. Geol. Surv. Open-File Report 94-431, U. S. Government Printing Office.

Hashash, Y.M.A. and D. Park (2001), Non-linear one-dimensional seismic ground motion propagation in the Mississippi embayment, Engn. Geol., 62, 185-206.

Haberland, C., and A. Rietbrock (2001), Attenuation tomography in the western central Andes: A detailed insight into the structure of a magmatic arc, J Geophys Res., 106, 11151-11167.

Hansen, S., C. Thurber, M. Mandernach, F. Haslinger, and C. Doran (2004), Seismic velocity and attenuation structure of the east rift zone and south flank of Kilauea volcano, Hawaii Bull. Seismo. Soc. Am., 94, 1430-1440.

Kang, I.B. and G. McMechan (1994), Separation of intrinsic and scatter Q based on frequency-dependent amplitudes of transmitted waves, J. Geophys. Res., 99, 32875-23885.

Langston, C.A. (2003), Local earthquake wave propagation through Mississippi embayment sediments, part II: influence of local site velocity structure on Qp-Qs determinations, Bull. Seismo. Soc. Am., 93, 2685-2702.

Langston, C.A., P. Bodin, C. Powell, M. Withers, S. Horton, and W. Mooney (2005), Bulk sediment Qp and Qs from explosion-generated seismic waves in the Mississippi embayment, Bull. Seism. Soc. of Am., 95, 2162-2179.

Lees, J. M. and G. T. Lindley (1994), 3-Dimensional Attenuation Tomography at Loma-Prieta - Inversion of T-Asterisk for Q, J. Geophys. Res., 99, 6843-6863.

Liu, Z., M.E. Wuenscher, and R.B. Herrmann (1994), Attenuation of Body Waves in the Central New Madrid Seismic Zone, Bull. Seismo. Soc. Am., 84, 1112-1122.

McKenna, J., S. Stein, and C.A. Stein (2007), Is the New Madrid seismic zone hotter and weaker than its surroundings? *In* S. Stein and S. Mazzotti ed. Continental Intraplate Earthquakes: Science, Hazard, and Policy Issues, GSA Special Paper 425, p. 167-175.

Newman, A., S. Stein, J. Weber, J. Engeln, A. Mao, and T. Dixon (1999). Slow deformation and lower seismic hazard at the New Madrid seismic zone, Science, 284, 619-621.

Powell, C.A., H.R. DeShon, and M. Withers (2010), Intrusions and Anomalous Vp/Vs Ratios Associated with the New Madrid Seismic Zone, *J. Geophys. Res.*, 115, B08311, doi:10.1029/2009JB007107.

Pujol, J. S. Pezeshk, Y. Zhang, and C. Zhao (2002), Unexpected values of Qs in the unconsolidated sediments of the Mississippi embayment, Bull. Seism. Soc. Am., 92, 1117-1128.

Rietbrock, A. (2001), P wave attenuation structure in the fault area of the 1995 Kobe earthquake, J. Geophys. Res., 106, 4141-4154.

Russ, D.P. (1982). Style and significance of surface deformation in the vicinity of New Madrid, Missouri: investigations of the New Madrid, Missouri, earthquake region, Geol. Surv. Profess. Pap. 1236, 95-114.

Stachnik, J., G. Abers, and D. Christensen (2004), Seismic attenuation and mantle wedge temperatures in the Alaska subduction zone, *J. Geophys. Res.*, 109, B10304, doi 10.1029/2004JB003018.

Thurber, C.H. (1983), Earthquake locations and three-dimensional crustal structure in the Coyote Lake area, central California, J. Geophys. Res., 88, 8226-8236.
Thurber, C., and D. Eberhart-Phillips (1999), Local earthquake tomography with flexible gridding, Computers Geosciences, 25, 809-818.
Tsumura, N., A. Hasegawa, and S. Horiuchi (1996), Simultaneous estimation of attenuation structure, source parameters, and site response spectra-Application to the northeastern part of Honshu, Japan, *Phys. Eart. Plan. Ints.*, 93, 105-121.
Tuttle, M.P., E.S. Schweig, J.D. Sims, R.H. Lafferty, L.W. Wolf, and M.L. Haynes (2002). The earthquake potential of the New Madrid seismic zone, Bull. Seism. Soc. Am 92, 2080-2089.
Zhang, H., and C.H. Thurber (2003), Double-difference tomography: method and application to the Hayward fault, California, Bull. Seismo. Soc. Am. 93: 1875–1889.